

# Vibration Analysis of Single-Phase Brushless DC Fan Drives Considering Position Signal Error

Nejat Saed , Graduate Student Member, IEEE, Shahin Asgari , Graduate Student Member, IEEE, and Annette Muetze , Fellow, IEEE

**Abstract**—Single-phase brushless DC machines find extensive application in automotive auxiliary drives due to their cost-effectiveness. However, compared to their three-phase counterparts, these machines exhibit higher levels of noise and vibration. Typically, single-phase brushless DC drives require a Hall-effect sensor to determine the motor's position to facilitate motor control. However, due to inherent manufacturing imperfections, the position signal may deviate from the zero-crossing points of the back-electromotive force, potentially affecting the switching angles and increasing the vibration of the machine. This paper identifies the optimal switching angles to mitigate vibration in single-phase brushless DC fan drives through analytical, numerical, and experimental investigations. To assess the position signal error, 56 fan drives have been experimentally analyzed to evaluate the sources of the error and its subsequent impact on vibration. Furthermore, through a comprehensive analysis, an optimal area of operation is proposed to minimize vibration at the critical frequency, ensuring robust performance against position signal error.

**Index Terms**—Single-phase brushless DC machines, vibration, position signal error, hall-effect sensor.

## I. INTRODUCTION

SINGLE-PHASE brushless DC (BLDC) machines are often favored over their three-phase counterparts in automotive auxiliary applications, specifically in systems like fans and pumps. This preference arises primarily due to cost considerations, which is the key design consideration in mass-produced fractional horsepower drives [1], [2]. However, single-phase permanent magnet machines possess inherent characteristics such as high cogging torque and torque ripple, which can make them more audible in comparison to the three-phase BLDC machines. Given the positioning of auxiliary drives in close proximity to

passengers, even minimal levels of noise and vibration have the potential to cause disruption [3].

Several noise and vibration mitigation techniques have been proposed for single-phase BLDC machines, as documented in the existing literature [4], [5], [6], [7], [8], [9], [10]. These techniques typically require rather complicated control strategies, which may not be suitable for cost-effective applications. Among these strategies are methods to reduce torque ripple through modified control techniques that regulate phase current [4] and incorporate additional voltage regulation circuits [5]. Control strategies targeting the reduction of commutation torque ripple have also been explored [6]. Furthermore, investigations have been conducted into modifying switching angles and avoiding current conduction when back-EMF is very low, with the objective of enhancing noise and vibration performance [7], [8]. Concurrently, structural modifications designed to mitigate noise and vibration have been examined [9], [10].

While BLDC machines offer advantages such as high power and torque density, low maintenance, and excellent controllability, effective control of BLDC motors typically necessitates the use of position sensors. It is worth noting that sensorless control schemes have also been developed with the aim of reducing the number of components required for position detection. However, these sensorless strategies tend to be more intricate and may lack the precision offered by sensor-based approaches [11], [12].

The choice of position sensor between resolvers, encoders, and Hall-effect sensors in speed variable drives depends on the application requirements. For instance, in robotic application, resolvers are preferred because of their resolution and robustness [13]. However, in low-cost single-phase BLDC drive systems, a simpler approach is adopted to employ only a single Hall-effect sensor to provide essential position information. This Hall-effect sensor is commonly mounted on the printed circuit board (PCB) and functions by detecting the leakage magnetic flux of the permanent magnet within the rotor [14]. Therefore, manufacturing imperfections within the permanent magnets, such as non-uniform magnetization, have the potential to compromise the precision of the position signal. Additionally, achieving precise sensor positioning on the PCB during the manufacturing process can prove challenging, further contributing to inaccuracies in position detection [15]. Although manufacturing imperfections can directly manifest as unbalanced magnetic force, thereby leading to noise and vibration concerns [16], [17], they may indirectly affect motor performance by introducing inaccuracies into the position signal.

Manuscript received 12 October 2023; revised 5 February 2024; accepted 17 March 2024. Date of publication 3 April 2024; date of current version 22 July 2024. Paper 2023-IDC-1239.R1, presented at the 2023 IEEE Workshop on Electrical Machines Design, Control and Diagnosis, Newcastle upon Tyne, U.K., Apr. 13–14, and approved for publication in the IEEE TRANSACTIONS ON INDUSTRY APPLICATIONS by the Industrial Drives Committee of the IEEE Industry Applications Society [DOI: 10.1109/WEMDCD55819.2023.10110902]. This work was supported in part by the Austrian Federal Ministry of Labor and Economy, and in part by the National Foundation for Research, Technology, and Development and the Christian Doppler Research Association. (Corresponding author: Nejat Saed.)

The authors are with the Christian Doppler Laboratory for Brushless Drives for Pump and Fan Applications, 8010 Graz, Austria and also with the Electric Drives and Power Electronic Systems Institute, Graz University of Technology, 8010 Graz, Austria (e-mail: nejat.saed@tugraz.at).

Color versions of one or more figures in this article are available at <https://doi.org/10.1109/TIA.2024.3384466>.

Digital Object Identifier 10.1109/TIA.2024.3384466

The impact of misaligned and unbalanced position signals on the performance of three-phase BLDC machines, as well as techniques for diagnosing and compensating for these errors have been investigated [18], [19], [20]. It has been highlighted that error in the position signal can decrease efficiency and increase low-frequency harmonics in the electromagnetic torque. These studies emphasize the impact of imprecise positioning of sensors, resulting in unbalanced Hall-effect sensor signals that are not in a  $120^\circ_{\text{elec}}$  relationship with each other. However, in single-phase BLDC machines, which utilize only one Hall-effect sensor, the main error is misalignment between the position signal and back electromotive force (back-EMF) zero-crossing points which has received comparatively less attention in the literature.

This paper provides a comprehensive expansion of the initial findings previously introduced in [1] and aims to propose a straightforward modification of the switching angles as a part of the control strategy to mitigate vibration in the drive system without incurring additional costs. It also extends the analysis of the impact of misaligned position signals on the performance of the fan drive beyond just two operating points to encompass the entire range of interest. This extended analysis involves the utilization of both finite element analysis (FEA), implemented through JMAG [21], and experimental measurements.

## II. METHODOLOGY

This study initially investigates the existence of position signal errors arising from different sources in an example case single-phase BLDC fan drive system. Therefore, Section III provides a brief introduction to the operation of the example case drive, and Section IV experimentally investigates position signal errors as provided by the Hall-effect sensors in 56 fan drives. The potential impact of these errors on the vibration arises from calculation of the switching angles, as this calculation relies on information from the Hall-effect position signal. Section V presents the results of the experimental investigations into the effect of position signal errors on vibration.

The following part of the paper, Section VI, comprehensively examines the effect of the switching angles on the vibration of the drive system and proposes an approach for determining the optimum switching angles to minimize the critical vibration harmonics. Furthermore, the effect of the position signal errors on the optimal area of operation is investigated to identify the resilient optimum switching angles.

## III. EXAMPLE CASE SINGLE-PHASE BLDC FAN DRIVE

Two main topologies of single-phase BLDC machines, i.e., salient-pole and claw-pole stator structures, are introduced for use in low-cost automotive applications [22], [23], with the choice between outer and inner rotor structures depending on the specific application requirements. The example case motor is shown in Fig. 1, which is a four-pole outer-rotor permanent magnet (PM) motor featuring a four-slot salient-pole stator with bifilar winding used in a radial fan for automotive auxiliary applications. The motor parameters are detailed in Table I.

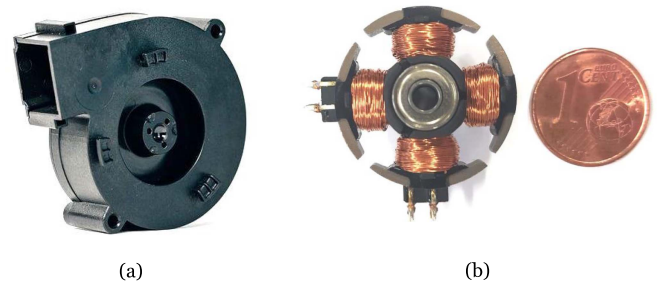


Fig. 1. (a) Example case radial fan drive equipped with a single-phase salient-pole BLDC machine, and (b) a prototype of the example case machine (stator and windings).

TABLE I  
PARAMETERS OF THE EXAMPLE CASE FAN DRIVE

Parameter	Value
$U_{DC}$	8–16 V
$\omega_{nom}$	5000 rpm
$T_{nom}$	1.54 mN·m
$R$	8.5 $\Omega$
$L_\sigma$	260 $\mu\text{H}$
$L_m$	2.8 mH

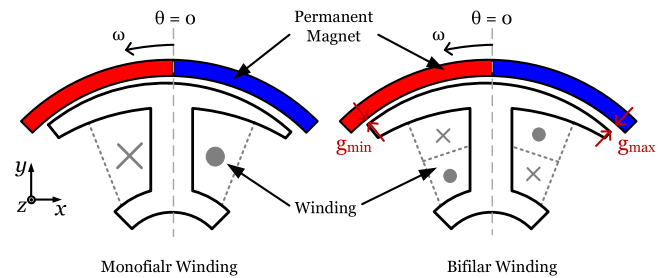


Fig. 2. Schematic of a single-phase BLDC machine with tapered air-gap profile and two winding configurations.

Details on the dynamic and steady-state operation of this drive can be found in [22].

Single-phase BLDC machines typically have the same number of slots and poles, resulting in a pulsating magnetic field that renders them incapable of generating starting torque [22], [23], [24]. To overcome this inherent limitation, an approach involving the introduction of an asymmetric magnetic flux density distribution along the airgap is used. This asymmetry facilitates the generation of starting torque in a desired direction [9], [25]. In the single-phase BLDC machine illustrated in Fig. 2, a tapered asymmetric air-gap profile is implemented, which generates starting torque in the counterclockwise direction.

Two distinct winding configurations are introduced for these machines, as illustrated in Fig. 2. Monofilar winding entails the use of one coil per stator tooth. In contrast, bifilar winding involves two sets of coils per stator tooth, wound in opposite directions. The required inverter for these configurations is determined by the fact that torque production in these machines relies on sequentially alternating the stator poles between north

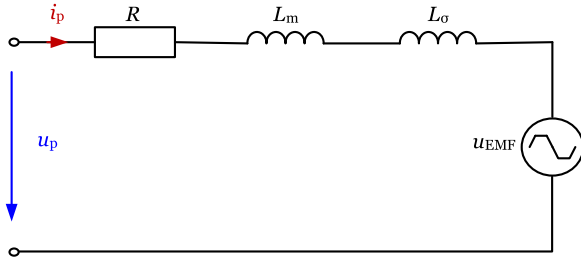


Fig. 3. Equivalent circuit of a single-phase BLDC motor with monofilar winding.

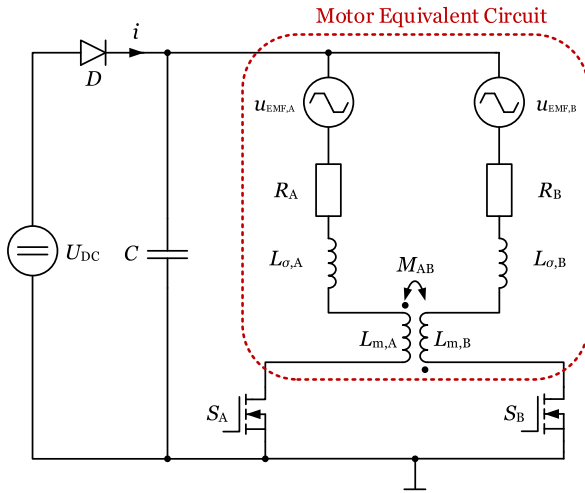


Fig. 4. Inverter circuit of a single-phase BLDC motor with bifilar winding.

and south poles by changing the current polarity in the winding over time. Consequently, a full bridge inverter is necessary to inject positive/negative current in the motor in the case of monofilar winding. However, bifilar winding only requires two power switches, as the injected current in the switches for both phases flows in the same direction, and the change in polarity is achieved through oppositely wound windings. Despite bifilar winding utilizing only half of the copper in the stator during each current conduction period, it is sometimes preferred over the monofilar configuration due to cost considerations arising from the reduced number of power electronic switches.

Fig. 3 provides a visualization of the equivalent circuit of a single-phase BLDC machine with monofilar winding featuring a trapezoidal-shaped back-EMF waveform, where  $R$  represents the phase resistance and  $L_m$  and  $L_\sigma$  denote the main and leakage inductances, respectively. The equivalent circuit for a single-phase BLDC motor with bifilar winding is depicted in Fig. 4, where the coupling between two coils is modeled with a mutual inductance,  $M$ . Due to the winding process wherein two windings are wound together, the coupling factor is between 0.8 and 1 [26]. Fig. 4 further illustrates the electronic circuit essential for commutating the phase current. The inverter components comprise a constant supply voltage  $U_{DC}$ , a diode  $D$  implemented to prevent the flow of regenerative energy back into the power

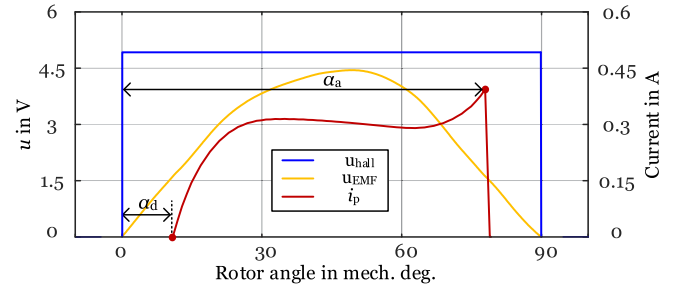


Fig. 5. Illustration of Hall-effect position signal in relation to back-EMF zero-crossing points and phase current.

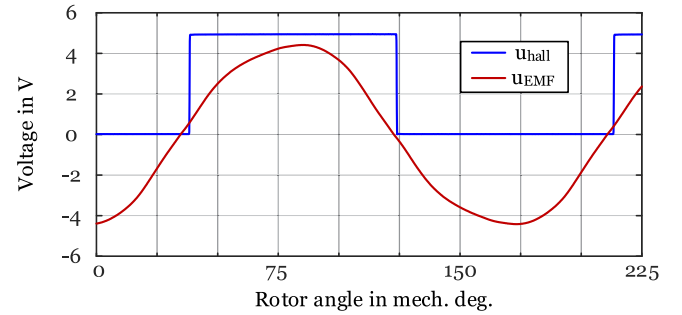


Fig. 6. Measured misaligned Hall-effect sensor signal respect to back-EMF of an example case drive system with  $3^\circ_{\text{mech}}$  misalignment.

source, a DC link capacitance  $C$ , and the commutation switches  $S_A$  and  $S_B$ .

#### IV. POSITION SIGNAL ANALYSIS

As illustrated in Fig. 5, the Hall-effect sensor detects the zero-crossing points of the back-EMF by generating a rising or falling voltage edge. These edges serve as references for calculating the advanced turn-off angle,  $\alpha_a$ , and delayed turn-on angle,  $\alpha_d$ . These angles are typically implemented to enhance the efficiency of the motor. However, the position signal may exhibit error when recognizing the zero-crossing points, like an example illustrated in Fig. 6. It demonstrates the misalignment of  $3^\circ_{\text{mech}}$  between Hall-effect sensor signal and zero-crossing points of the back-EMF.

The error in the position signal can be attributed to various sources, including signal analysis error, Hall-effect sensor inaccuracies, or manufacturing imperfections. However, in mass-produced sub-fractional horsepower electric drives, where manufacturing imperfections are virtually unavoidable, this error can typically be traced back to two primary factors: sensor mispositioning and the non-uniform magnetization pattern of the permanent magnets within the rotor.

##### A. Sensor Mispositioning

Achieving an accurate position signal requires precise positioning of the Hall-effect sensor on the PCB to detect polarity changes of the magnetic flux at the back-EMF zero-crossing points. Consequently, determining the sensor's location should

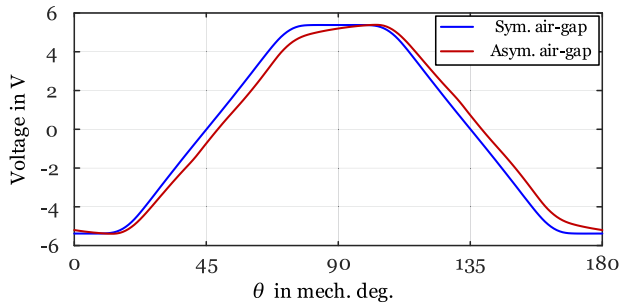


Fig. 7. Simulated back-EMF waveforms of two cases of the single-phase BLDC motors with symmetric and asymmetric air-gap profiles.

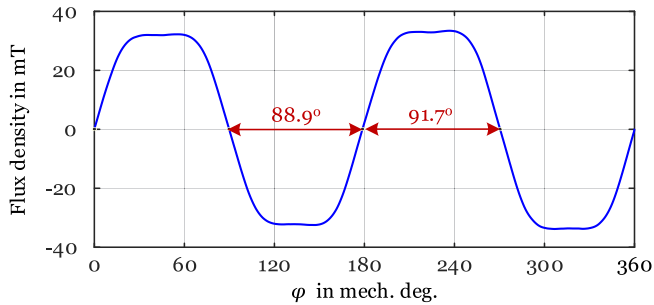


Fig. 8. Measured magnetic flux density along circumference of a ring permanent magnet of the example case motor.

take into account the stator's topology and the characteristics of the air-gap profile.

The rotor position in Fig. 2 is considered as  $\theta = 0$ , where  $\theta$  represents the rotor angle with respect to the defined reference. If the air-gap profile is symmetric, a zero-crossing point of the back-EMF occurs after a  $45^\circ_{\text{mech}}$  rotation of the rotor, as depicted in Fig. 7. In this scenario, if the Hall-effect sensor is positioned at the middle of the slot opening, i.e.,  $\theta = 45^\circ_{\text{mech}}$ , it detects the polarity change of the magnet poles simultaneously with the zero-crossing point of the back-EMF. However, in the case of a single-phase BLDC machine with an asymmetric air-gap, the zero-crossing points of the back-EMF waveform are shifted compared to the machine with symmetric air-gap, as shown in Fig. 7. Therefore, if the sensor is located at the same position as in the machine with a symmetric air-gap, a misalignment error in the position signal occurs.

### B. Non-Uniform Magnetization

As an illustration of imperfections in magnetization, Fig. 8 displays the magnetic flux density measured along the circumference of an example ring permanent magnet where  $\varphi$  is the angular coordinate. The flux density of the permanent magnet is measured using a Hall-effect sensor mounted on a plastic cylinder which is positioned within the rotor, replacing the stator. Then, the rotor is rotated by an external mover and the signal of the Hall-effect sensor is recorded. In this depiction, there is an evident discrepancy of approximately  $3^\circ_{\text{mech}}$  between the magnetization of two consecutive poles. This magnetization error directly impacts the signal generated by the Hall-effect

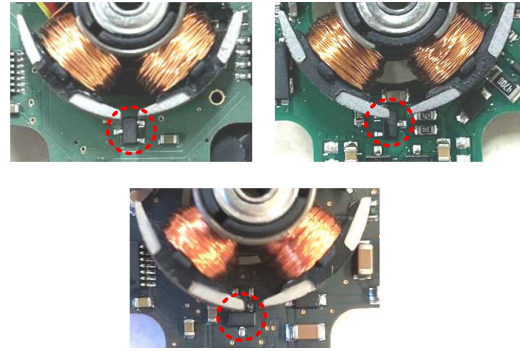


Fig. 9. Three example cases of single-phase BLDC machines with different positioning of the Hall sensor (marked by red circles) on the PCB.

TABLE II  
MEASURED POSITION ERROR FROM 3 PCBs, EACH OPERATING 18 DIFFERENT ROTORS

PCB number	Position error (mech. deg.)		
	Minimum	Average	Maximum
1	5.1	7.0	8.4
2	0.4	1.4	3.2
3	0.7	2.9	4.6

sensor, given that one pole is longer than the other, leading to variations in the sensor's output signal.

The variation in magnetization between different poles does indeed impact the position signal detection, resulting in asymmetry within the signal. However, this asymmetry is not reflected in the back-EMF of the machine as proved in the Appendix, leading to misalignment between the Hall-effect sensor signal and zero-crossing points of the back-EMF.

### C. Experimental Position Signal Analysis

In order to analyze the position signal error related to sensor mispositioning and non-uniform magnetization, 56 combinations of three distinct PCB layout designs, as shown in Fig. 9, each featuring a Hall-effect sensor positioned slightly differently and 18 different rotors are examined.

In this experiment, the fan impeller is rotated by an external mover to generate back-EMF in the terminal of the motor, and it is measured simultaneously with the output signal of the Hall-effect sensor. An example of the measurement results is shown in Fig. 6, and quantitative results are summarized in Table II.

The findings indicate that error in the placement of Hall-effect sensors lead to an offset error up to  $7^\circ_{\text{mech}}$  or  $14^\circ_{\text{elec}}$  in the results depending on the sensor's position. However, variations in the magnetization of the permanent magnet across different rotors induce a varying error in the position signal of approximately  $3^\circ_{\text{mech}}$ . While the error associated with sensor mispositioning can be minimized through precise PCB design, the error arising from magnetization imperfections is randomly distributed.

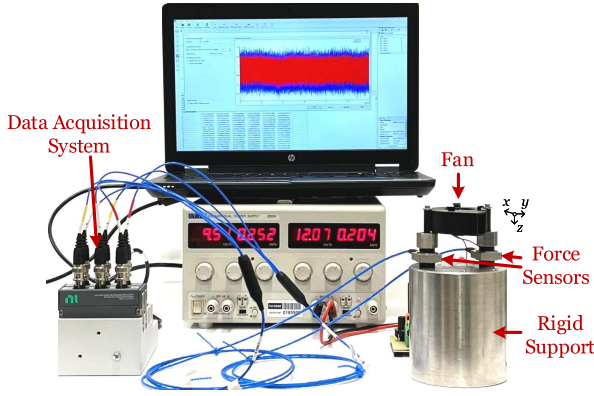


Fig. 10. Vibration measurement setup.

## V. THE EFFECT OF POSITION SIGNAL ERROR ON THE VIBRATION

In single-phase BLDC machines, conducting close to the back-EMF zero-crossing points not only does not generate a significant amount of torque but also increases current peaks which raises electromagnetic forces and reduces efficiency. Consequently, modified switching strategies have been introduced to enhance motor performance. These strategies involve advancing the turn-off angle and delaying the turn-on angle of the switching [see  $\alpha_a$  and  $\alpha_d$  in Fig. 5] to mainly reduce copper losses and improve overall motor efficiency [7], [8], [27].

In this section, the impact of variations in these switching angles resulted from position signal error on the vibration of the example case drive system is investigated.

### A. Vibration Measurement Setup

The measurement setup involves two triaxial force sensors, 260M36 model from PCB Piezotronics [28], and the fan system is mounted on a rigid support that is significantly heavier than the fan drive, as depicted in Fig. 10. This vibration measurement set-up is based on the VW 82469 standard [29], which is one of the few industrial standards for noise and vibration of small electric drives. The sensors' data are collected with a high precision data recorder cDAQ-9174 [30] and two NI-9232 measurement cards [31] from National Instruments. As per the standard's specifications, measured forces from all attachment points are summed up and presented in one-third octave band analysis.

Furthermore, the standard defines three limitation curves for force, depending on the application of the drive system, within the frequency range of 10 to 1000 Hz as follow

- *Limit 1:* passenger-operated auxiliary drives which are activated when the combustion engine is *on*.
- *Limit 2:* passenger-operated auxiliary drives which are activated when the combustion engine is *off* and those which operate automatically when the combustion engine is *on*.
- *Limit 3:* automatic auxiliary drives when the combustion engine is *off*.

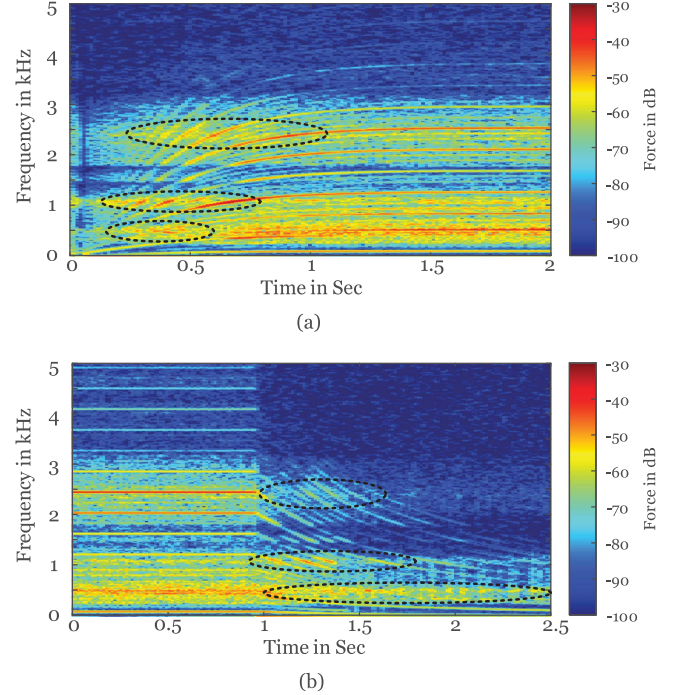


Fig. 11. Extraction of natural frequencies through (a) run-up and (b) cast-down tests.

### B. Natural Frequencies of the Drive System

Resonance between electromagnetic forces and the natural frequencies of the mechanical structure is one of the main sources of noise and vibration in electric machines. To identify the natural frequencies of the example case fan drive, vibration measurements are conducted during the motor's run-up to the speed of 6000 rpm and subsequent cast-down to standstill. The results of this experiment are presented in the spectrograms shown in Fig. 11, where dashed lines indicate the approximate times of resonance occurrences.

The measurements are performed at a standard sampling frequency of 51.2 kHz, and spectrograms are generated using a Hanning window with a 75% overlap. Three significant resonances around 500, 1100, and 2500 Hz are consistently observed in both experiments, resonating with multiple magnetic force harmonics upon crossing these frequencies.

### C. Vibration Analysis

To assess the impact of position signal error on vibration performance, four different error cases including  $e = \pm 2^\circ_{\text{mech}}$  and  $\pm 4^\circ_{\text{mech}}$ , representing lagging and leading position signal error, are applied to the fan drive. For instance, for a given operating point  $(\alpha_d, \alpha_a)$ , a lagging error of  $2^\circ_{\text{mech}}$  shifts the switching angles to  $(\alpha_d + 2, \alpha_a + 2)$ , while a leading error of  $2^\circ_{\text{mech}}$  shifts them to  $(\alpha_d - 2, \alpha_a - 2)$ .

Fig. 12 compares the one-third octave band analysis of the measured forces with the example switching angles of  $(\alpha_d, \alpha_a) = (9^\circ_{\text{mech}}, 74^\circ_{\text{mech}})$  and applied errors at a nominal speed of 5000 rpm.

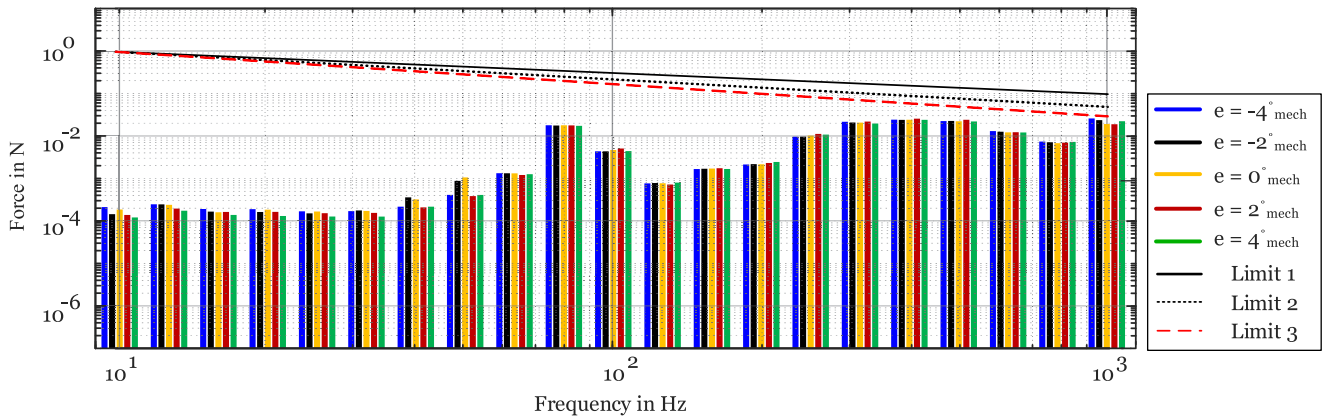


Fig. 12. One-third octave band analysis of the vibration of the example case drive for an operation point considering leading and lagging position signal error.

Among the harmonics in the one-third octave band, those at frequencies of 79 Hz, 1000 Hz, and in the range of 300 to 500 Hz exhibit the highest amplitudes. The 79 Hz harmonic closely aligns with the first harmonic of the magnetic forces, with an actual frequency of 83.33 Hz, representing the unbalanced magnetic force in the machine, which is typically elevated in these machines due to manufacturing imperfections. On the other hand, the fourth harmonic of forces at 333.33 Hz, which is the main harmonic of the magnetic forces due to the slot/pole combination of the machine [3], and a resonance around 500 Hz contribute to high measured forces in the 300 to 500 Hz range. Additionally, the side-band effect of the unbalanced magnetic force amplifies adjacent harmonics around the fourth harmonic, i.e., the third and fifth harmonics, influencing the force values in this frequency range. Also, the force harmonic at 1000 Hz corresponds to the 12th harmonic of the magnetic forces at the nominal speed and is in the proximity to the natural frequency of the system around 1100 Hz.

It can be observed from Fig. 12 that the maximum force variation resulting from applying position signal error occurs at the frequency of 1000 Hz, approaching the maximum allowable value per the standard. This highlights the importance of the variations in the electromagnetic forces due to position signal error, although the adjacent resonance close to this frequency can also impact the force amplitude. The results indicate that a  $+2^{\circ}_{\text{mech}}$  position signal error decreases this force harmonic by 1.3%, whereas a  $+4^{\circ}_{\text{mech}}$  error increases the force by 16.3%. Moreover,  $-2^{\circ}_{\text{mech}}$  and  $-4^{\circ}_{\text{mech}}$  errors raise the force by 23.8% and 26.3%, respectively.

Fig. 13 displays the input current waveform of the drive system at switching angles of  $(9^{\circ}_{\text{mech}}, 74^{\circ}_{\text{mech}})$  and the aforementioned four other error cases. The figure illustrates that the current waveform and its peak change with the switching angles. Leading position error increases the first peak of the current, while lagging position error increases the second peak, altering the harmonic content of the current and also affecting the efficiency of the drive system [32].

The measurement results underline that even a minor misalignment between the position signal obtained from a Hall-effect sensor and the back-EMF can lead to a significant increase in vibration at the critical frequency of 1000 Hz. However, the

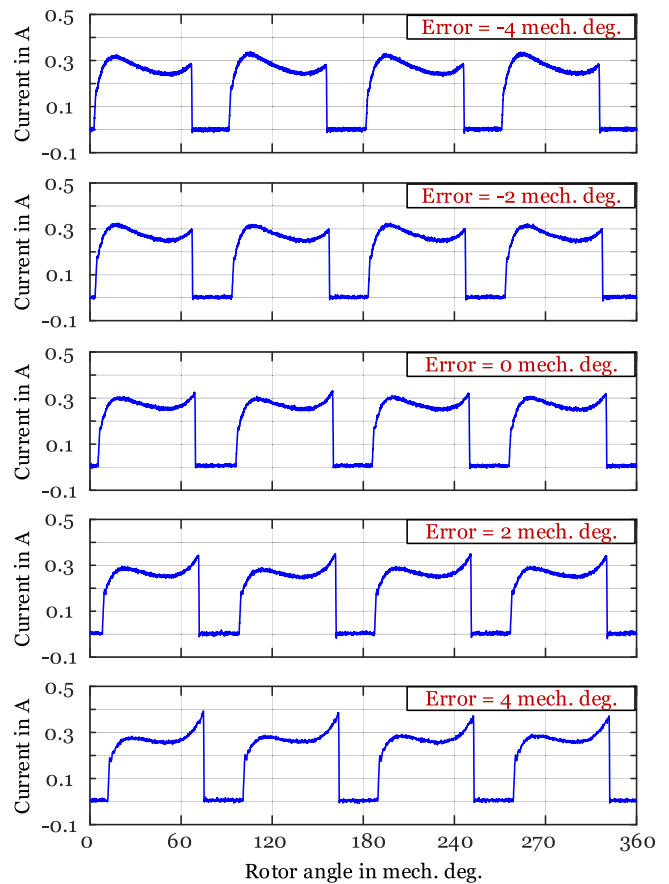


Fig. 13. Measured input current for an operation point considering leading and lagging position signal error.

relation between vibration and error in the switching angles cannot be identified by only a few sets of switching angles. A comprehensive analysis covering a wide range of switching angles has been conducted and is reported in the next section of this paper.

## VI. SWITCHING ANGLES OPTIMIZATION

To extend the initial experimental investigations in previous section to a wider range of switching angles, a complementary

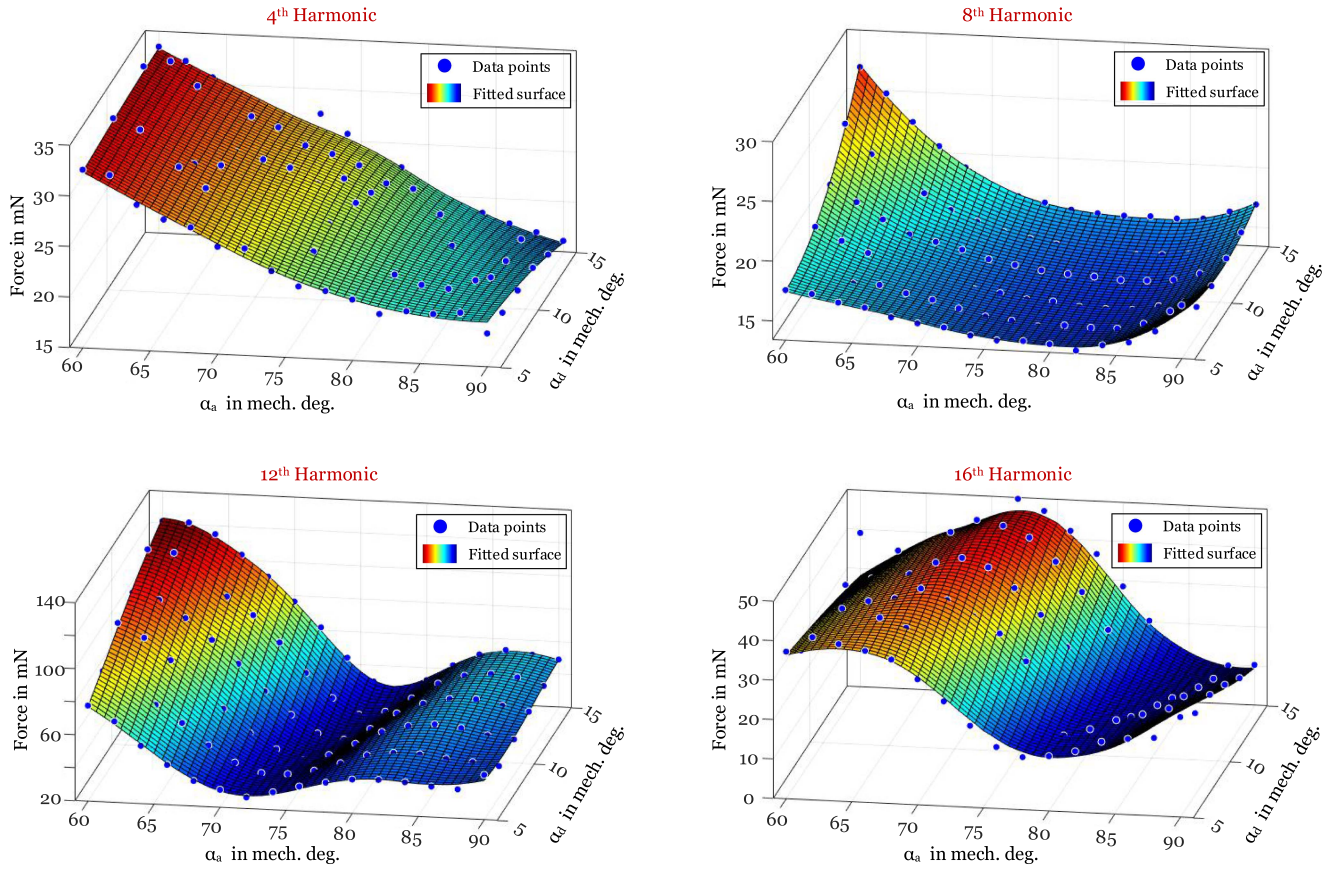


Fig. 14. Measured forces at different harmonics for the example case drive with variation of the switching angles.

experiment is performed involving a change in the turn-off angle,  $\alpha_a$ , ranging from  $60^\circ_{\text{mech}}$  to  $90^\circ_{\text{mech}}$ , and a variation in the turn-on angle,  $\alpha_d$ , from  $5^\circ_{\text{mech}}$  to  $15^\circ_{\text{mech}}$ . This limitation for  $\alpha_d$  arises from the fact that, at the nominal speed of the machine, the used low-cost microprocessor cannot operate below  $5^\circ_{\text{mech}}$  due to its processing speed constraints.

Fig. 14 presents the measured forces at four frequencies within the one-third octave band spectrum which are close to main harmonics of the magnetic forces. These frequencies include 316, 630, 1000, and 1258 Hz, which are the closest frequencies to the 4th, 8th, 12th and 16th harmonics of the forces at nominal speed, respectively. It is worth noting that while the 16th harmonic falls outside the standard's range of interest for the fan at nominal speed, this harmonic can be shifted to frequencies below 1000 Hz as the speed decreases.

The results reveal that variations in switching angles lead to significant changes in the amplitudes of dominant force harmonics. Among these harmonics, the 12th harmonic exhibits the most significant variation in amplitude, potentially causing the force to exceed the specified limit in the standard, which is around 30 mN for Limit 3. The measured data for the 12th harmonic demonstrates that the fan drive can only meet the standard's requirements within a limited range of operational switching angles. However, the amplitudes of the other harmonics remain below the allowable values for all three limitation curves across the entire operational range.

To analyze the sources of 12th harmonic of the measured forces, contours of this harmonic of torque from the 3-dimensional FEA of the machine and measured phase current are depicted in Fig. 15. In the FEA, the turn-off and turn-on angles vary from  $60.5^\circ_{\text{mech}}$  to  $86.5^\circ_{\text{mech}}$  and  $5.5^\circ_{\text{mech}}$  to  $13.5^\circ_{\text{mech}}$ , respectively.

A comparison of the 12th harmonic in the force, torque, and input current, as illustrated in Figs. 14 and 15, reveals that the force variation exhibits a closer resemblance to current than to torque variations. Notably, force variations nearly track torque variations within the range of approximately  $\alpha_a = 60^\circ_{\text{mech}}$  to  $75^\circ_{\text{mech}}$ . However, beyond this range, while the amplitude of the 12th harmonic of torque continues to decrease, the measured forces at the same frequency experiences an increase.

The reduction in torque harmonic, concurrent with an increase in current, can be attributed to the phenomenon that current near the zero-crossing point of the back-EMF does not significantly contribute to torque production. Additionally, as the conduction period from  $\alpha_d$  to  $\alpha_a$  widens, the torque waveform approaches a constant value, leading to a reduction in the amplitude of all harmonics.

In essence, while the 12th harmonic of current at higher  $\alpha_a$  switching angles may not directly impact the torque harmonics, it can generate magnetic forces in the machine, resulting in vibration. Consequently, the reduction in current harmonics can contribute to vibration reduction at the desired frequency.

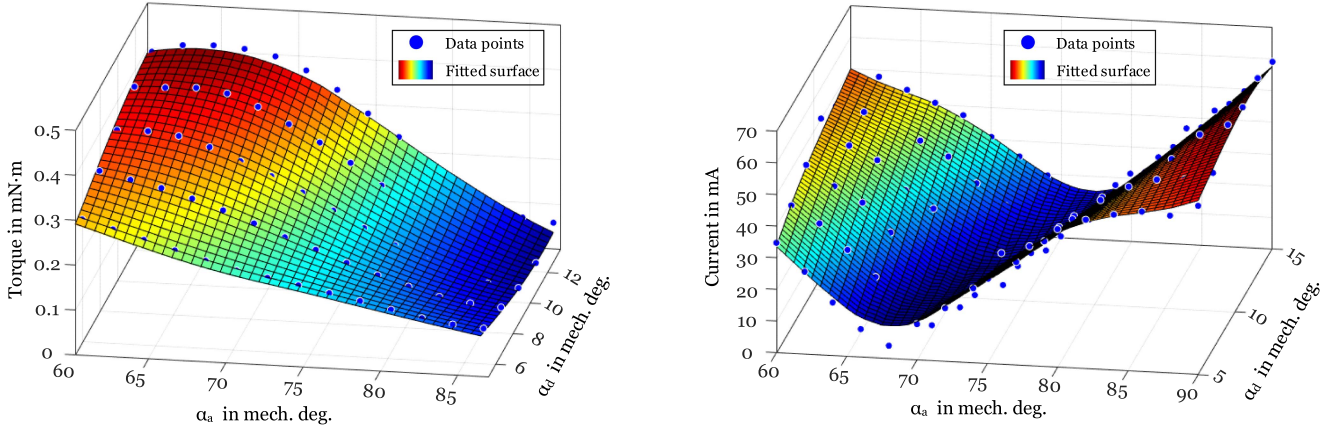


Fig. 15. Simulated torque and measured current at 1000 Hz (12th harmonic) with variation of the switching angles.

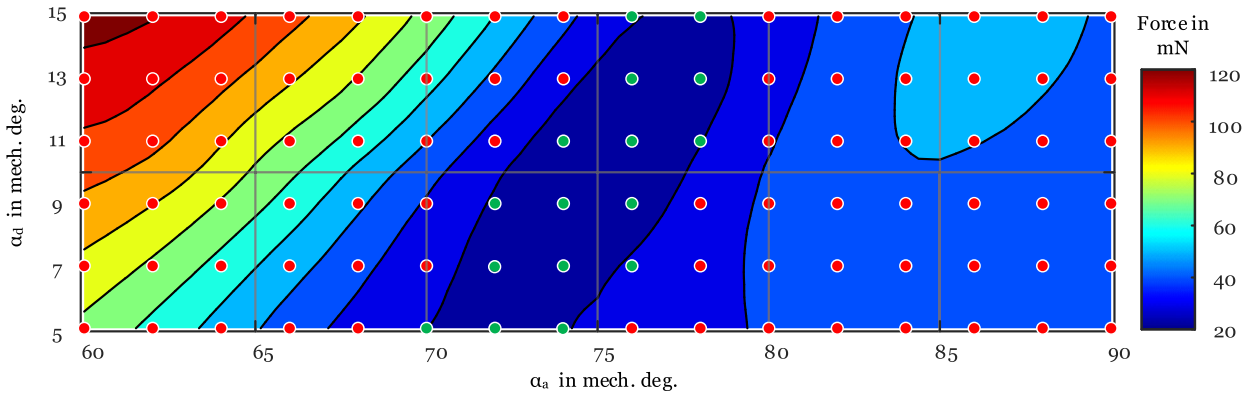


Fig. 16. 2-dimensional contour of measured 12th harmonic of the forces.

### A. Current Harmonics Mitigation

If the typical current waveform of single-phase BLDC machine, like current waveform in Figs. 5 and 13, is considered as a constant current  $A$  between the switching angles of  $\alpha_d$  and  $\alpha_a$  within a  $90^\circ_{\text{mech}}$  period, it can be expressed as follows

$$i_p(t) = \begin{cases} A, & \alpha_d \leq \alpha \leq \alpha_a \\ 0, & \text{otherwise,} \end{cases} \quad (1)$$

The Fourier series of the current can be written as

$$i_p(t) = \sum_{n=0}^{\infty} I_n \cos(n\omega t + \phi_n). \quad (2)$$

Where the amplitude of each current harmonic,  $I_n$ , can be written as

$$I_n = 2 \frac{A}{n\pi} \sin(2n(\alpha_a - \alpha_d)). \quad (3)$$

This equation illustrates that variations in  $\alpha_d - \alpha_a$  can lead to the cancellation of certain harmonics in the current waveform. For instance, if  $\alpha_d - \alpha_a = \frac{k\pi}{6}$ , the third harmonic of current,  $I_3$ , becomes zero. Since these equations are derived to describe the current function in (1), and there are four consecutive instances of this waveform in each rotation of the rotor, the third harmonic in this function corresponds to the 12th harmonic of the phase current.

This analysis elucidates the approximate region where the 12th harmonic of both vibration and phase current in Figs. 14 and 15 are minimized, which occurs when  $\alpha_d - \alpha_a \approx \frac{\pi}{3}$ . Similar behavior is observed for the 4th and 16th harmonics of forces in Fig. 14, where  $\alpha_d - \alpha_a$  approaches  $\frac{\pi}{2}$  and  $\frac{3\pi}{8}$ , respectively. However, because the conduction period in the experiment does not fully cover the range of  $\alpha_d - \alpha_a \approx \frac{\pi}{4}$ , which is necessary to minimize the vibration of the 8th harmonic, and because the frequency corresponding to this harmonic in the one-third octave band analysis is not an exact match with the harmonic frequency, this effect is not visible for the 8th harmonic. Additionally, as the amplitude of this harmonic is significantly lower compared to other harmonics, the influence of side-band harmonics resulting from unbalanced magnetic forces can dominate the measured force values [16].

Based on these analytical investigations, it can be concluded that the optimized switching angles to minimize challenging vibration frequencies at any operating point in a single-phase BLDC fan drive can be calculated from (3). However, it is important to consider other effects resulting from the variation of switching angles, such as efficiency. For instance, when  $\alpha_d - \alpha_a = \frac{\pi}{6}$ , the 12th harmonic of the current is still theoretically minimized, however, the efficiency is significantly lower in this case compared to  $\alpha_d - \alpha_a = \frac{\pi}{3}$  due to the need for a much higher current in a shorter current conduction period to produce the same amount of torque.

A comprehensive study on the impact of varying switching angles on the efficiency of single-phase BLDC fan drives has been conducted in [32]. This study can be combined with the findings presented here to select the optimal switching angles for achieving the desired drive performance while considering both vibration mitigation and high efficiency.

### B. Switching Angles Selection Considering Position Signal Error

Fig. 16 presents a 2-dimensional contour plot of the measured 12th harmonic of the forces in Fig. 14, making it easier to visualize the effect of position signal error. The operation points that meet the requirements of Limit 3 of the standard are colored in green, while those that do not are colored in blue. Among all investigated switching angle sets, only three sets can stay below the limit of the standard with  $\pm 4^\circ_{\text{mech}}$  position signal error which are  $(7^\circ_{\text{mech}}, 74^\circ_{\text{mech}})$ ,  $(9^\circ_{\text{mech}}, 74^\circ_{\text{mech}})$ , and  $(13^\circ_{\text{mech}}, 76^\circ_{\text{mech}})$ . These switching angles are the most resilience operation points against the maximum varying error measured in Section IV.

Among these three operation points,  $(7^\circ_{\text{mech}}, 74^\circ_{\text{mech}})$  has the highest efficiency at 52.6%, followed by  $(9^\circ_{\text{mech}}, 74^\circ_{\text{mech}})$  at 52.0%, and  $(13^\circ_{\text{mech}}, 76^\circ_{\text{mech}})$  at 51.7%. However,  $(9^\circ_{\text{mech}}, 74^\circ_{\text{mech}})$  exhibits the best vibration performance with its 12th harmonic force amplitude being 19.2% lower than  $(7^\circ_{\text{mech}}, 74^\circ_{\text{mech}})$  and 4.6% lower than  $(13^\circ_{\text{mech}}, 76^\circ_{\text{mech}})$ . Therefore, the choice between these switching angles for the drive system depends on the preference for either better efficiency or vibration performance.

## VII. CONCLUSION

This paper builds upon the findings presented in [1] and extends the analysis to investigate the impact of switching angles and position signal error in a broader range of operating points. In the initial part of the paper, experimental investigations are carried out on a total of 56 fan drive systems to assess the sources of misaligned position signals related to Hall-effect sensors. The results reveal two significant sources of error: a varying error of approximately  $3^\circ_{\text{mech}}$  attributed to non-uniform magnetization and an offset error of up to  $7^\circ_{\text{mech}}$  associated with sensor mispositioning.

In the subsequent section of the paper, a comprehensive experimental study is conducted to explore the influence of varying switching angles on the vibration characteristics of the example case single-phase BLDC fan drive system. The findings indicate that the most critical frequency in the vibration spectrum is 1000 Hz, where the amplitude of this harmonic exhibits significant variability with changes in the switching angles. This variation has the potential to elevate the force harmonic beyond the limits defined by an industrial standard.

Furthermore, based on experimental findings and analytical analyses, an approach is proposed to select the switching angles with the objective of minimizing specific current and force harmonics. Additionally, optimal switching angles are identified, exhibiting greater resilience against potential position signal error, ensuring compliance with allowable vibration limits as defined by the relevant standard.

## APPENDIX

Assuming a conventional monofilar single-phase winding of a salient-pole stator with  $Q$  slots, like the example with  $Q = 4$  shown in Fig. 17, regardless of magnetization imperfections in the rotor, the induced voltage in the coil 1 can be written as a Fourier series as

$$E_{C1} = \sum_{n=0}^{\infty} E_n \cos(n\omega t + \phi_n). \quad (4)$$

If the stator is ideally symmetric, the induced voltage on other coils can be determined based on their mechanical angle respect to coil 1 and the winding direction which defines the polarity of induced voltage respect to reference coil 1 as

$$E_{C2} = - \sum_{n=0}^{\infty} E_n \cos\left(n\left(\omega t + \frac{1}{Q}2\pi\right) + \phi_n\right), \quad (5)$$

$$E_{C3} = \sum_{n=0}^{\infty} E_n \cos\left(n\left(\omega t + \frac{2}{Q}2\pi\right) + \phi_n\right), \quad (6)$$

$$E_{C4} = - \sum_{n=0}^{\infty} E_n \cos\left(n\left(\omega t + \frac{3}{Q}2\pi\right) + \phi_n\right). \quad (7)$$

Therefore, the induced voltage on each coil can be written as

$$E_{Ci} = (-1)^{i-1} \sum_{n=0}^{\infty} E_n \cos\left(n\left(\omega t + \frac{i-1}{Q}2\pi\right) + \phi_n\right), \quad (8)$$

which in the case of the example case motor with four slots is

$$E_{Ci} = (-1)^{i-1} \sum_{n=0}^{\infty} E_n \cos\left(n\left(\omega t + \frac{i-1}{2}\pi\right) + \phi_n\right). \quad (9)$$

The total induced voltage on the phase is the summation of the induced voltage of all coils, given by

$$E_{\text{tot}} = \sum_{i=1}^Q E_{Ci}. \quad (10)$$

By importing (9) in (10), the total induced voltage for the example case machine is derived as

$$E_{C1} + E_{C3} = \sum_{n=0}^{\infty} 2E_k \cos(k\omega t + \phi_k), k = 2n, \quad (11)$$

$$E_{C2} + E_{C4} = - \sum_{n=0}^{\infty} 2E_k \cos\left(k\left(\omega t + \frac{\pi}{2}\right) + \phi_k\right), k = 2n, \quad (12)$$

$$E_{\text{tot}} = \sum_{n=0}^{\infty} 4E_k \cos(k\omega t + \phi_k), k = 4n + 2. \quad (13)$$

In the example case machine where the fundamental harmonic of the back-EMF is  $n = 2$ , corresponding to the number of pole-pairs, only odd harmonics can result in unbalanced zero-crossing points of the back-EMF. On the other hand, the phase back-EMF equation in (13) shows that in the example case machine, only even harmonics appear in the Fourier series, while all odd harmonics are canceled out. Therefore, as long as the

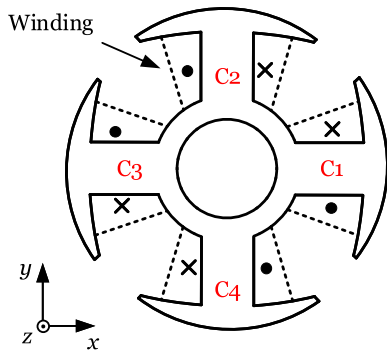


Fig. 17. Monofilar winding of a salient-pole single-phase BLDC machine.

amplitude of the fundamental harmonic significantly exceeds that of other harmonics, which is typically the case, the sequential zero-crossing points of the phase back-EMF consistently maintain a  $180^\circ_{\text{elec}}$  phase difference, even if the zero-crossing points of the magnetic flux exhibit asymmetry like the case depicted in Fig. 8.

#### ACKNOWLEDGMENT

The authors would like to express their appreciation to Dr. Felix Krall and MSG Mechatronic Systems GmbH, Wies, Austria for their valuable contributions during the design and prototyping stages. ChatGPT 3.5 [33] has been used for editing and grammar enhancement of the paper. The paper has been subsequently edited manually again.

#### REFERENCES

- [1] N. Saed, S. Asgari, and A. Muetze, "On the effect of position signal error on the performance of single-phase BLDC drives," in *Proc. IEEE Workshop Elect. Machines Des., Control Diagnosis*, 2023, pp. 1–6.
- [2] A. Muetze, S. Leitner, H. Gruebler, and F. Krall, "Performance improvements of auxiliary drives for automotive pump and fan applications," *Elektrotechnik und Informationstechnik*, vol. 137, pp. 226–234, 2020.
- [3] N. Saed, S. Leitner, F. Krall, and A. Muetze, "Noise and vibration characteristics of sub-fractional horsepower single-phase BLDC drives," *e i Elektrotechnik und Informationstechnik*, vol. 139, pp. 260–270, 2022.
- [4] W. Lee, J. H. Kim, W. Choi, and B. Sarlioglu, "Torque ripple minimization control technique of high-speed single-phase brushless DC motor for electric turbocharger," *IEEE Trans. Veh. Technol.*, vol. 67, no. 11, pp. 10357–10365, Nov. 2018.
- [5] H.-J. Hu, G.-Z. Cao, S.-D. Huang, C. Wu, and Y.-P. Peng, "Drive circuit-based torque-ripple suppression method for single-phase BLDC fan motors to reduce acoustic noise," *IET Electric Power Appl.*, vol. 13, pp. 881–888, 2019.
- [6] S.-Y. Jung, Y.-J. Kim, J. Jae, and J. Kim, "Commutation control for the low-commutation torque ripple in the position sensorless drive of the low-voltage brushless DC motor," *IEEE Trans. Power Electron.*, vol. 29, no. 11, pp. 5983–5994, Nov. 2014.
- [7] L. Sun, Q. Feng, and J. Shang, "Drive of single-phase brushless DC motors based on torque analysis," *IEEE Trans. Magn.*, vol. 43, no. 1, pp. 46–50, Jan. 2007.
- [8] C.-L. Chiu, Y.-T. Chen, Y.-L. Liang, and R.-H. Liang, "Optimal driving efficiency design for the single-phase brushless DC fan motor," *IEEE Trans. Magn.*, vol. 46, no. 4, pp. 1123–1130, Apr. 2010.
- [9] Y.-U. Park, J.-H. Cho, and D.-k. Kim, "Cogging torque reduction of single-phase brushless DC motor with a tapered air-gap using optimizing notch size and position," *IEEE Trans. Ind. Appl.*, vol. 51, no. 6, pp. 4455–4463, Nov/Dec. 2015.
- [10] C.-T. Liu, Y.-M. Chen, and A. Homg, "Vibration reduction of a single-phase spindle motor with structural refinement," in *Proc. IEEE APMRC*, 2010, pp. 1–2.
- [11] G.-J. Su and J. McKeever, "Low-cost sensorless control of brushless DC motors with improved speed range," *IEEE Trans. Power Electron.*, vol. 19, no. 2, pp. 296–302, Mar. 2004.
- [12] S. Ogasawara and H. Akagi, "An approach to position sensorless drive for brushless DC motors," in *Proc. Conf. Rec. IEEE Ind. Appl. Soc. Annu. Meeting*, 1990, pp. 443–447.
- [13] M. Bourogaoui, H. B. A. Sethom, and I. S. Belkhdja, "Speed/position sensor fault tolerant control in adjustable speed drives – A review," *ISA Trans.*, vol. 64, pp. 269–284, 2016.
- [14] A. Sikora, A. Zielonka, and B. Kulesz, "Impact of hall sensors positioning on symmetry of BLDC control signals," in *Proc. Int. Symp. Power Electron. Power Electron., Elect. Drives, Automat. Motion*, 2012, pp. 249–252.
- [15] D. A. Papatanasopoulos and E. D. Mitronikas, "Diagnosis of defective hall-effect position sensors in brushless DC motor drives," in *Proc. IEEE Workshop Elect. Machines Des., Control Diagnosis*, 2019, pp. 137–142.
- [16] N. Saed, S. Leitner, and A. Muetze, "Effect of the interaction of different manufacturing imperfections on the unbalanced radial forces in a sub-fractional HP single-phase BLDC motor," in *Proc. IEEE Energy Convers. Congr. Expo.*, 2021, pp. 3690–3696.
- [17] S. Leitner, H. Gruebler, and A. Muetze, "Effects of manufacturing imperfections and design parameters on radial magnetic forces in the BLDC claw-pole motor," in *Proc. IEEE Int. Electric Machines Drives Conf.*, 2019, pp. 2167–2173.
- [18] N. Samoylenko, Q. Han, and J. Jatskevich, "Dynamic performance of brushless DC motors with unbalanced hall sensors," *IEEE Trans. Energy Convers.*, vol. 23, no. 3, pp. 752–763, Sep. 2008.
- [19] P. Alaeinovin, S. Chiniforoosh, and J. Jatskevich, "Evaluating misalignment of hall sensors in brushless DC motors," in *Proc. IEEE Canada Electric Power Conf.*, 2008, pp. 1–6.
- [20] Q. Zhang and M. Feng, "Combined commutation optimisation strategy for brushless DC motors with misaligned hall sensors," *IET Electric Power Appl.*, vol. 12, pp. 301–307, 2018.
- [21] JSOL Corporation, "Simulation technology for electromagnetical design," 2023. Accessed: Oct. 10, 2023. [Online]. Available: <http://www.jmag-international.com/>
- [22] S. Dunkl, A. Muetze, and G. Schoener, "Design constraints of small single-phase permanent magnet brushless DC drives for fan applications," *IEEE Trans. Ind. Appl.*, vol. 51, no. 4, pp. 3178–3186, Jul./Aug. 2015.
- [23] S. Leitner, H. Gruebler, and A. Muetze, "Innovative low-cost sub-fractional HP BLDC claw-pole machine design for fan applications," *IEEE Trans. Ind. Appl.*, vol. 55, no. 3, pp. 2558–2568, May/Jun. 2019.
- [24] S. Leitner, N. Saed, and A. Muetze, "Novel bent steel sheet strip based two-pole single-phase BLDC motor topology for low-cost fan applications," in *Proc. IEEE Energy Convers. Congr. Expo.*, 2021, pp. 3993–3999.
- [25] B.-I. Kwon, B.-Y. Yang, S.-C. Park, and Y.-S. Jin, "Novel topology of unequal air gap in a single-phase brushless DC motor," *IEEE Trans. Magn.*, vol. 37, no. 5, pp. 3723–3726, Sep. 2001.
- [26] S. Leitner, "Low-cost sub-fractional HP outer-rotor BLDC claw-pole motor designs with reduced cogging torque," Ph.D. dissertation, Electric Drives and Machines Institute, Graz University of Technology, Graz, Austria, 2020.
- [27] W. Cui, Y. Gong, and M. H. Xu, "A permanent magnet brushless DC motor with bifilar winding for automotive engine cooling application," *IEEE Trans. Magn.*, vol. 48, no. 11, pp. 3348–3351, Nov. 2012.
- [28] PCB Piezotronics, "Triaxial force sensor 260M36," 2022. Accessed: Jan. 9, 2024. [Online]. Available: [https://www.pcbpiezotronics.de/produkte/datenblatt/?untergruppe=kra\\_triach&h=PCB&m=260M36](https://www.pcbpiezotronics.de/produkte/datenblatt/?untergruppe=kra_triach&h=PCB&m=260M36)
- [29] F. Bieler, "Zusatzaggregate – Akustische Anforderungen," Volkswagen Konzernnorm, VW 82 469 2014.
- [30] National Instruments, "cDAQ-9174," 2023. Accessed: Jan. 9, 2024. [Online]. Available: <https://www.ni.com/de-at/shop/model/cdaq-9174.html>
- [31] National Instruments, "NI-9232," 2023. Accessed: Jan. 9, 2024. [Online]. Available: <https://www.ni.com/de-at/shop/model/ni-9232.html>
- [32] H. Gruebler, S. Leitner, A. Muetze, and G. Schoener, "Improved switching strategy for a single-phase brushless direct current fan drive and its impact on efficiency," *IEEE Trans. Ind. Appl.*, vol. 54, no. 6, pp. 6050–6059, Nov./Dec. 2018.
- [33] OpenAI, "ChatGPT 3.5," 2024. Accessed: Jan. 9, 2024. [Online]. Available: <https://chat.openai.com/>